



Available online at [www.sciencedirect.com](http://www.sciencedirect.com)



Mechanism and Machine Theory 00 (2024) 1–20

Mechanism  
and  
Machine  
Theory

## A novel stiffness-controllable joint using antagonistic actuation principles

Wenlong Gaozhang<sup>1</sup>, Yue Li<sup>2</sup>, Jialei Shi<sup>1</sup>, Yaxi Wang<sup>1</sup>, Agostino Stilli<sup>3</sup>, Helge Wurdemann<sup>1</sup>

<sup>1</sup> Department of Mechanical Engineering, University College London, UK.

<sup>2</sup>School of Biomedical Engineering & Imaging Sciences, King's College London, UK.

<sup>3</sup>Department of Medical Physics and Biomedical Engineering, University College London, UK.

---

### Abstract

The inherent safety of collaborative robots is essential for enhancing human-robot interaction. The primary challenge in creating soft components for these robots is achieving sufficient force and stiffness. This paper presents a joint design for collaborative robots that addresses this challenge by incorporating an antagonistic actuation principle, allowing for adjustable stiffness. The novelty of our variable-stiffness joint lies in achieving a wide range of stiffness variation at any bending angle through antagonistic actuation. This bio-inspired principle results from the activation of two opposing actuation chambers. Compared to existing joints, our proposed joint is compact and utilises a high percentage of soft materials, enabling safer human-robot interaction. The paper outlines the joint's design and fabrication process, highlighting the feasibility of our innovative concept. Kinematic and stiffness models are introduced to analyze the bending and stiffness characteristics, which are further validated through experimental testing. The stiffness experiments demonstrate significant stiffness changes achievable through the antagonistic actuation principle. Additionally, force experiments reveal our joint can generate 20 N force at a  $1.5 \times 10^5$  Pa pressure. A constant force output experiment confirms the joint's advantages in providing consistent force compared to motors. Finally, a case study showcases how our proposed joint can be embedded in serial robots with variable stiffness capabilities under loading and safe human-robot interaction.

© 2011 Published by Elsevier Ltd.

**Keywords:**

Soft robot materials and design, Human-Robot Interaction, soft joint, variable stiffness, collaborative robots.

---

### 1. Introduction

Collaborative robots, or cobots, are becoming more prevalent in the industry due to their ability to increase productivity and efficiency. However, it is necessary to ensure humans remain safe when working in the same space as robots [1]. Therefore, several methods have been developed to ensure safe human-robot interaction.

One method involves distributed force or current sensors integrated in the joints or links of a robot. Motors located in the joints react if the sensors detect a physical interaction/collision by reducing the output force or stopping the robot's motion. These techniques are employed in cobots produced by companies such as UR (Denmark) [3], OMARON (UK) [4], and Franka Emika (Germany) [5]. Although this method has been demonstrated as efficient and accurate due to the use of mature sensor and motor control technology, risks to humans remain when relying solely on software-based safety measures [6]. Another method for creating safer collaborative robots is using elastic components such as springs to create variable stiffness in robotic joints. By setting a stiffness value, the output force of the joint can be assigned to a maximum limit, which prevents the robot from causing severe damage if a collision

occurs. For instance, Variable Stiffness Joints (VSJ) have been researched based on torsion springs [7, 8, 9], leaf springs [10, 11, 12], magnetic springs [13, 14], and artificial muscle [15, 16, 17]. Although joints with elastic parts can reduce harm, the weight and rigidity of the robotic components result in limited safety for close human-robot interactions.

Substituting rigid components with soft parts to construct variable stiffness components, such as inflatable links or air pressure-driven joints, is another potential solution. For instance, a number of studies have investigated variable stiffness links that can change their stiffness by controlling the interior air pressure to allow for safe human-robot interaction [18, 19, 20, 21]. Several air-driven joints have been developed to replace traditional joints; these typically have two chambers with a rigid rotational component. Examples of this include the joints of a Festo Bionic-Cobot [22], the hybrid joints applied in minimally invasive surgery [23], and a joint based on a pneumatic actuator [24, 25, 26, 27, 28]. Jamming mechanisms also offer effective way in modulating the stiffness of compliant joints and grippers [29, 30, 31, 32, 33]. Particle jamming, for instance, involves a mass of particles that transition between fluid-like and solid-like states by changing the volume or pressure, allowing for dynamic adjustment of stiffness [31, 33]. Similarly, layer jamming uses multiple thin, flexible layers that become rigid when their relative movement is constrained [29, 30, 32]. By employing a specifically designed jamming structure in conjunction with various driving sources, such as positive pressure, vacuum, magnetic fields, or voltage, it is possible to effectuate an efficient and broad-range alteration in the stiffness of these joints and grippers. On the other hand, the concept of antagonistic actuation is deployed in soft robotic manipulators to allow on-demand stiffness [34, 35, 36, 37, 38, 39]. Inspiration is taken from biological systems involving pairs of muscles that work in opposition to each other. This mechanism is able to achieve motion and capable to adjust stiffness in a precise manner. In the human arm shown in Fig. 1(a), for instance, the simultaneous activation of the biceps and triceps can vary the elbow joint's stiffness without changing its position, enabling the arm to stabilise objects or apply controlled force. Similarly, in octopuses, the complex interplay between longitudinal, transverse, and oblique muscle groups allows for adjustments in arm stiffness, supporting precise manipulation tasks and dynamic interaction with the environment. This principle of using antagonistic action to modulate stiffness provides a versatile strategy for designing robotic systems capable of sophisticated and adaptive interactions, mirroring the nuanced capabilities observed in nature.

However, several critical gaps remain. For instance, the antagonistic actuation behavior of the joint has not been evaluated experimentally and theoretically [24, 27]. The dimensions, structure, and control strategies of existing concepts are not specifically designed and optimized for being a joint used in collaborative robots, as reported in [40, 27, 29]. Moreover, the percentage of the soft material is not sufficient to guarantee inherent safety, like the joints proposed in papers [23, 24].

Building on our previous research creating Variable Stiffness Link collaborative robots [18, 19, 20], this paper

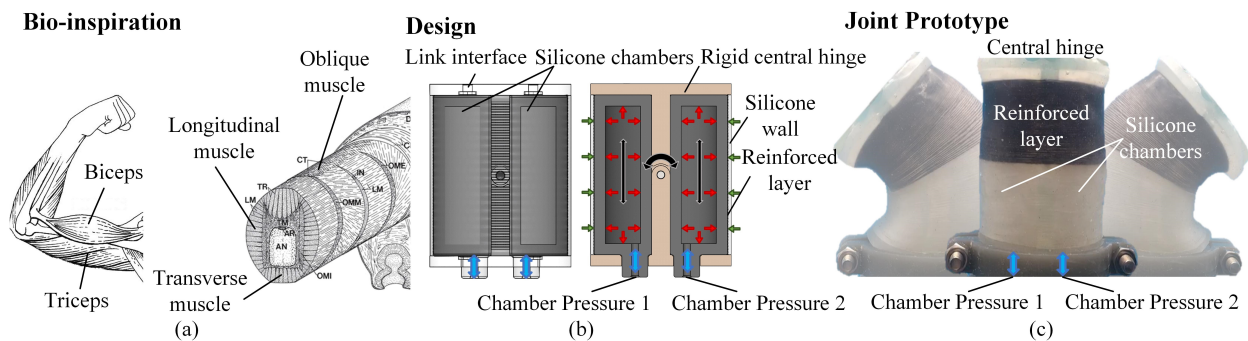


Figure 1. (a) Inspiration of the antagonistic actuation principle from biology: In the human arm (left), the simultaneous activation of the biceps and triceps can vary the elbow joint's stiffness without changing its position, enabling the arm to stabilise objects or apply controlled force. In octopuses (right), the complex interplay between longitudinal, transverse, and oblique muscle groups allows for adjustments in arm stiffness [2]. (b) Design and working principle of the stiffness-controllable joint: this prototype has a height of 49 mm and a diameter of 38 mm with two semi-circular pressurized chambers. The cross-sectional view illustrates how the inner pressure acts on the soft material shell, which is reinforced by unidirectional fabric. A central hinge limits the bending motion of the chamber to allow rotation around a fixed axis. Simultaneous actuation of both chambers changes the rotational stiffness based on an antagonistic actuation principle. (c) The joint prototype is constructed from two colours of reinforcement fabric thread to indicate the top and bottom of the joint.

proposes a new design for soft joints with variable stiffness based on an antagonistic actuation principle (see Fig. 1). The novelty and innovation of our variable-stiffness joint for collaborative robots lies in achieving a wide range of stiffness variation at any bending angle through antagonistic actuation. This bio-inspired principle results from the activation of two opposing actuation chambers as shown in Fig. 1(a). In particular, our joint is based on two inflatable chambers (chamber pressure 1 and 2), a unidirectional reinforcement layer, and a central hinge as shown in Fig. 1(b). Symmetrically placed air chambers constructed from silicone material can control the direction and bending angle of the joint. Through antagonistic actuation of both chambers, it is possible to control the rotational stiffness of the joint, demonstrated in Fig. 1(c). The central hinge limits the bending motion of the chamber to allow rotation around a fixed axis. The fabric unidirectional reinforcement layer limits the extension at the diameter direction of the chamber, which also provides high affordability of the chamber in terms of air pressure. The fabric layer and the central rigid hinge cocooned by a silicone chamber provide the joint with a higher load capacity and a wider stiffness range compared to joints composed solely of soft material. By using a high proportion of soft materials without a rigid outer shell, the design of this joint would allow inherently safer interaction between a collaborative robot and a human. The new design of the stiffness controllable soft joint proposed in this paper makes the following contributions to the field of soft robotics:

- The compact structure and dimensions are more suitable to replace the traditional joint of collaborative robot when compared to joints found in the literature [40, 25].
- The joint is built with a high percentage of soft material, which promises greater inherent safety than similar joints [24].
- The proposed kinematic and stiffness models are verified to evaluate the joint behaviour caused by the antagonistic actuation principle.

The structure of this paper is as follows: Section 2 presents the design of the soft joint and its fabrication process. Section 3 focuses on the modeling of kinematics and stiffness. The experimental setup, protocols, and results are described in Section 4. In Section 5, a robot equipped with the proposed joints is showcased, demonstrating its variable stiffness capabilities and safe human-robot interaction scenarios. Finally, Section 6 provides a summary of the conclusions and achievements of this research, along with the future work.

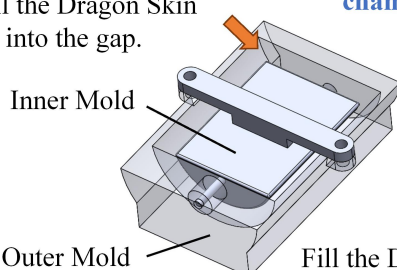
## 2. Design, fabrication and control system of joint prototype

Our stiffness-controllable soft joint is constructed using three main structural elements: a rigid central hinge, silicone air chambers, and a fibre-reinforced silicone layer. As shown in Fig. 1(b), the two pneumatic chambers are symmetrically placed on the two sides of the hinge, and the two ends of these chambers are connected with the two ends of the hinge. When one of the pneumatic chambers is pressurised, the chamber expands. As a result, the expanding air chamber pushes the end of the hinge and produces torque around the shaft. To prevent the radial extension of the chamber, unstretchable thread (0.2 mm diameter) is twined around the chambers; the surface of the fibre is covered with silicone rubber to fix each loop in place, allowing the thread to extend evenly in the axial direction. The reinforced silicone layer is then able to limit the radial expansion of the chamber, ensuring that most of the force generated by the interior air pressure of the chamber can be used to bend the joint.

The molding process of each chamber can be summarised as follows: to manufacture the enclosed silicone rubber chamber, we used a multi-step approach and designed several molds as shown in Fig. 2. Firstly, we designed the inside and outside molds for a semi-circular chamber as shown in Fig. 2(a). Since half of a chamber is an open structure, it is possible to remove the inside mold after the silicone rubber has cured. The semi-circular chamber is then put on the bottom mold, which was also filled with silicone rubber liquid (see Fig. 2(b)). After the chamber bottom cured, the entire enclosed silicone rubber chamber is formed. We investigated several commercially available silicone rubbers and compared the properties in terms of the elongation rate, hardness, and stress-stretch curve.[27] We also produced chamber samples with several types of silicone rubbers to determine the most suitable material for the joint. As a result, we found that Dragon Skin 20 from Smooth-On Inc. (Macungie, PA, US) has a 620 % elongation rate, 20 A shore hardness, and more than 40 MPa tensile stress at break. Its hardness and relatively high tensile stress at break

### Fabrication Process

Fill the Dragon Skin 20 into the gap.



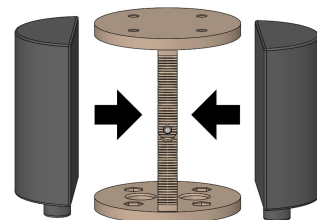
Molding chambers

Fill the Dragon Skin 20 into bottom mold.

(a)

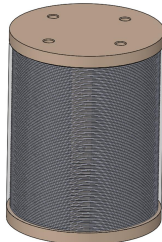
Mounting chambers

Central Hinge



(b)

Completed prototype



(e)

Creating outside wall



(d)

Soak joint in the cup and take out for curing.



(c)

Creating reinforced layer

0.2mm Diameter Thread

Figure 2. The fabrication process of the joint prototype: (a) The molding process of the enclosed chamber. The gap of the semi-circular chamber mold is filled with Dragon Skin 20. (b) Once de-molded, the bottom mold is filled with Dragon Skin 20. The processed chamber is put on the surface of the Dragon Skin 20, resulting in one closed semi-circular chamber. (c) A chamber is loaded on each side of the hinge. (d) An unstretchable 0.2 mm diameter cotton thread is twined around the circumference of the chambers. (e) The joint is dipped into a cup filled with Ecoflex 10 silicone for 1 min, and (f) cured.

compared with other silicone rubbers ensure that the wall will not break, leak, or balloon in small areas when the chamber is inflated with pressurised air.

As shown in Fig. 2(c), (d), (e), and (f), we positioned the chambers on each side of the hinge. The unstretchable thread (0.2 mm diameter cotton) was twined circle by circle around the two chambers to build the reinforcement layer. The main function of the outer wall is to fix every circle of the thread in place, so we use the silicone Ecoflex 00-10 (Smooth-On Inc.) with a 0-10 shore hardness. The whole joint is soaked in Ecoflex 00-10 liquid three times during the pot time (30 min) and then hung to cure for 240 min, allowing the silicone rubber liquid to evenly cover the surface of the joint via gravity and create a 1 mm wall. Fig. 1(c) shows the physical joint prototype. As shown in Fig. 3, the system to actuate the bending movement of the soft joints consists of two pressure regulators K8P-0-E522-0, (Camozi, Nuneaton, UK), a voltage regulator, a 24 V power source, a compressor for supplying air pressure, and a PC-based Data Acquisition (National Instruments, Mopac Expwy, Austin) to provide the PWM while receiving the pressure feedback from the pressure regulators. This system manages the air pressure in each chamber of the joint to control the bending angle and the bending direction. The two videos provided as supplementary material to this submission show how this prototype is actuated.

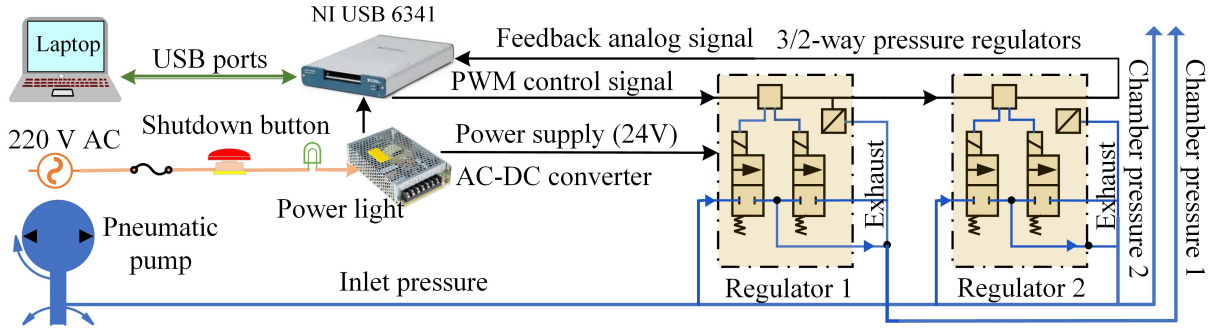


Figure 3. The control system consists of control components (pressure regulators and a voltage regulator), data processing components (NI PC-Based DAQ), a power source (24 V), and a pressure source (pneumatic pump).

### 3. Modelling the variable stiffness joint

The kinematic model and stiffness model capture the direct relationship between the input pressure in the two chambers and the bending angle by considering both the hyper-elastic material property of silicone rubber and the geometry of the joint. In addition, these models identify the stiffness behaviour at different bending angles and pressure. The variables in the model are the parameter and material properties that could be either measured or obtained from calibrations.

#### 3.1. Hyper-elastic material model

The proposed joint is fabricated using Dragon Skin 20 silicone rubber. Referring to the analysis of this material's characteristics [41], the Neo-Hookean (NH) model has the minor Akaike information criterion (AIC) compared to other hyper-elastic models like Mooney-Rivlin, Yeoh, Ogden, or Humphrey. Therefore, the incompressible NH hyper-elastic material model is used here to build the model of the chamber material. The strain energy is given in Eq. (1).

$$W = \frac{\mu}{2}(I - 3) \quad (1)$$

$$I = \sum \lambda_i^2$$

where  $I$  is the first invariant of the three (axial, circumferential, and radial) principal stretch ratios  $\lambda_1$ ,  $\lambda_2$  and  $\lambda_3$  and  $\mu$  is the initial shear modulus of the material. The principal nominal stresses  $s_i$  can then be obtained as a function of  $W$ ,  $\lambda_i$ , and the Lagrange multiplier  $p$  as in Eq. (2).

$$s_i = \frac{\partial W}{\partial \lambda_i} - \frac{p}{\lambda_i}. \quad (2)$$

#### 3.2. Kinematics model

The chamber with the reinforced layer will only extend along the axial direction when inflated with compressed air due to the limiting functions of the fibre-reinforced mechanism and central hinge. The extended chamber will then push the top of the central hinge and generate torque to the bending axis, leading to a bending angle. Although the actuator has a multilayered structure, for the sake of simplicity, it was modelled as a homogeneous incompressible NH material with effective initial shear modulus  $\bar{\mu}$ . The dynamics associated with pressurisation were neglected in the model.

The stretch along the axial direction of the chamber is denoted as the principal stretch  $\lambda_1$ . Furthermore, due to the fiber reinforcement constraint, the strain in the circumferential direction is negligible so that  $\lambda_2 = 1$ . Finally, considering the incompressibility of the material,  $\lambda_1 \lambda_2 \lambda_3 = 1$ . Next, we assumed the stress in the radial direction through the thickness of the actuator is 0, so  $s_i$  could result in Eq. (3).

$$s_i = \frac{\partial W}{\partial \lambda_i} - \frac{p}{\lambda_i} = \bar{\mu}(\lambda - \frac{1}{\lambda^3}) \quad (3)$$

When the chamber is inflated with compressed air, the pressure extends the area of the cavity cross-section from a semi-circular shape to nearly oval. It is assumed that the area of the cavity cross-section is linearly related to the pressure and  $a_0$  can be calibrated with the experimental data. The final area of the cavity cross-section of the two chambers  $A_1, A_2$  is determined by  $A_{p_i} = A_{p_0} + a_0 P_i$ , and  $A_{p_0} = b^2 \cdot \arccos(\frac{b}{t+a-b})$ , where  $A_{p_0}$  is the initial area of the cavity cross-section of chamber; it can be calculated by the geometrical relationship. The force generated by the compressed air can then be calculated by  $F_{p_i} = P_i \cdot A_{p_i}$ . The internal stretch of the extension in the axial direction results in an opposing force  $F_i = s_l \cdot A_i$ , where  $A_i = a^2 \cdot \arccos(\frac{t}{a}) - b^2 \cdot \arccos(\frac{b}{t+a-b})$  is the area of the chamber wall cross-section and  $\lambda_l, s_l$  are the main strain and stress along the axial direction. During bending, the elongation along the outside wall is different from the inside wall, so the central value  $\bar{l} = a \cdot \tan(\frac{\theta}{2}) + L$  is used to represent the average elongation of the whole chamber. Due to the geometric limitation of the central hinge, the geometries of the extended chamber can be simplified to be two straight lines that run parallel to the hinge.

Here, if it is assumed that there is no resistance from the folded chamber on the other side,  $F_i + F_{p_2} = F_{p_1}$ . However, in reality, folding of one side of the chamber causes resistance that is positively related to bending angle  $\theta$  to the extension of the other side chamber. For simplification, we assume that the resistant force  $f = n_1 \theta^{n_2}$  is proportional to the resistance coefficient  $n_1$  and  $n_2$ . According to the geometries shown in Fig. 4 (a) and (b), for joints in equilibrium, the force will be related as shown in Eq. (4).

$$F_{p_1} - F_{p_2} = F_i + f. \quad (4)$$

According to Eqs. (1) - (4), the relationship between the bending angle  $\theta$  and compressed air pressure  $P_1$  and  $P_2$  is

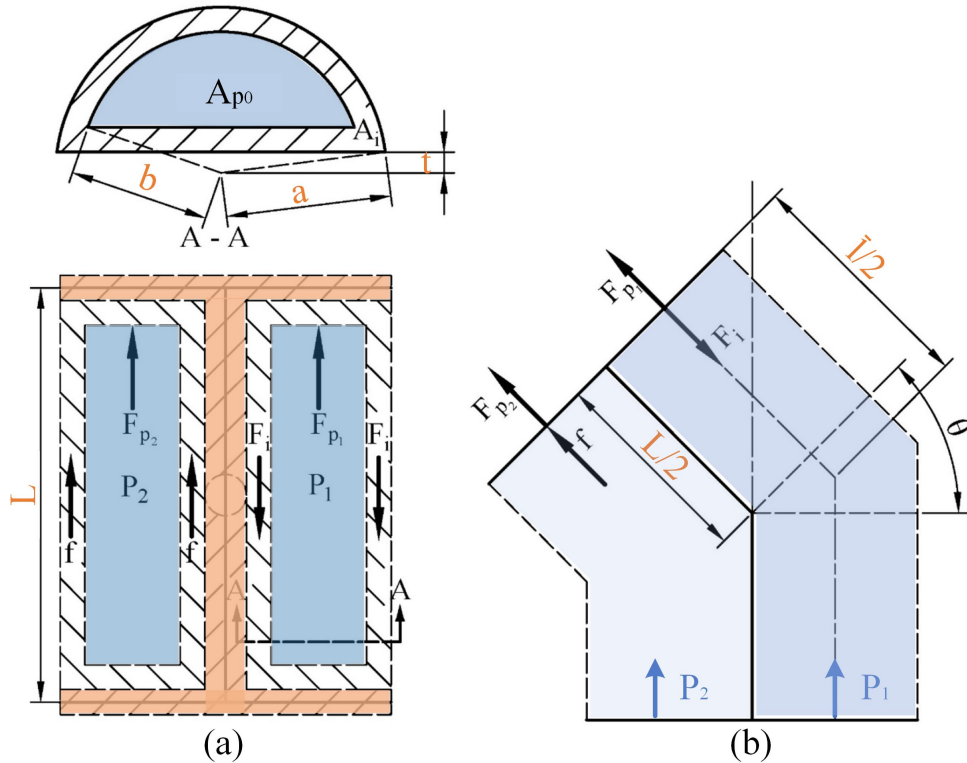


Figure 4. (a) Simplified geometrical structure of the soft joint, where the  $F_i$  represents the stretch stress of the extended chamber, and  $F_{p_1}$  and  $F_{p_2}$  are the force generated by the compressed air. The  $f$  represents the resistance force caused by the folding of another chamber. The cross-sectional view of the silicone rubber chamber shows the area of the cavity of the chamber  $A_{p_0}$  and the  $A_i$  is the area of the cross-section of the chamber. (b) Geometrical relationship of the joint at the bending angle  $\theta$ .

shown in Eq. (5).

$$n_0(P_1^2 - P_2^2) + A_{p_0}(P_2 - P_1) = A_i \bar{u} \left( 1 + \frac{a}{L} \tan\left(\frac{\theta}{2}\right) \right) - 1 / \left( 1 + \frac{a}{L} \tan\left(\frac{\theta}{2}\right) \right)^3 + n_1 \theta^{n_2}, \quad (5)$$

where  $n_0$ ,  $n_1$  and  $n_2$  are coefficients determined by the calibration,  $A_{p_0}$ ,  $A_i$ ,  $a$  and  $L$  are the design parameters, and  $\bar{u}$  is the material property.

### 3.3. Variable stiffness model

For establishing the stiffness of the joint prototype, it is assumed as a torsion spring, with the stiffness of the joint defined in Eq. (6).

$$K = \frac{M}{\Delta\theta}. \quad (6)$$

According to the above equation and Fig. 5 (a) and (b), the equilibrium when the external torque is applied to the bending centre of the joint is determined by Eq. (7).

$$(F_{p_1} - F_i(\theta + \Delta\theta))L_m + M = M_r(\theta + \Delta\theta). \quad (7)$$

According to Eqs. (6) and (7), the stiffness of the joint  $K$  can be represented in Eq. (8).

$$K(\theta) = \frac{M_r(\theta + \Delta\theta) - (F_{p_1} - F_i(\theta + \Delta\theta))L_m}{\Delta\theta}, \quad (8)$$

where  $F_{p_1} - F_i(\theta + \Delta\theta)$  has been identified in the section of the bending angle model, and  $M_r(\theta + \Delta\theta)$  is the resistant torque of the compressed chamber at the bending angle of  $\theta + \Delta\theta$ . It is a function of the bending angle and the internal pressure, so it can be represented by  $M_r(\theta, P_c)$ , where  $P_c$  is the internal pressure of the compressed chamber.  $M_r(\theta, P_c)$  consists of the linear torque  $M_r(P_c)$  generated by the pressure and a non-linear torque  $M_r(\theta)$  generated by the inflated semi-circular beam (i.e. the silicone chamber). Therefor we can get the  $M_r(P_c) = \frac{1}{2}(m_1 P_c + m_2)L$ , where  $m_1, m_2$  can

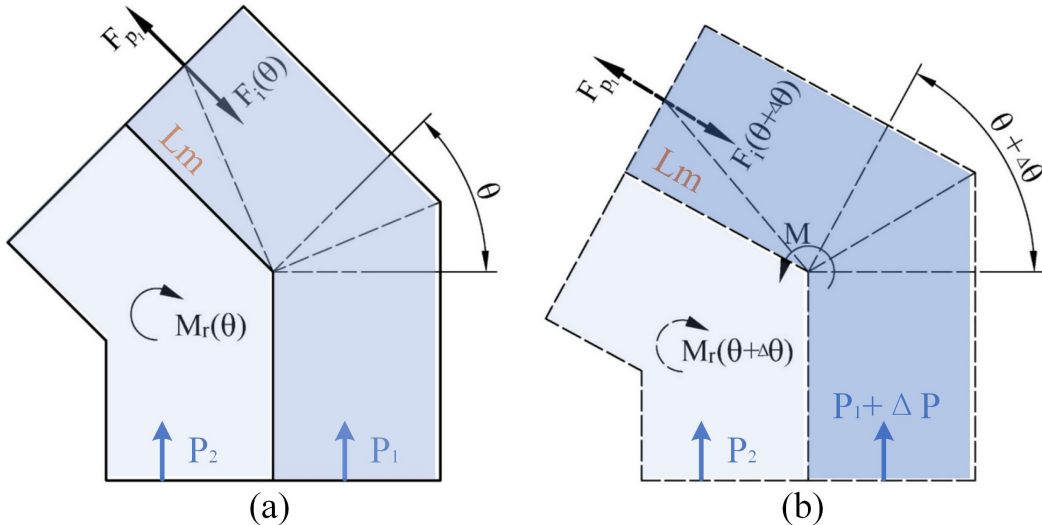


Figure 5. (a) and (b) Geometric model for establishing the stiffness model, where the  $F_i$  represents the stretch stress of the extended chamber, and  $F_{p_1}$  is the force generated by the compressed air.  $M_r$  is the resistant torque generated by the compressed chamber,  $\theta$  represents the bending angle, and  $\Delta\theta$  is the change of the bending angle generated by the external torque  $M$ .

be found with the calibration data. Since  $M_r(\theta)$  is a non-linear torque, it can be defined as a Fourier expansion, see Eq. (9).

$$M_r(\theta) = \frac{1}{2}(a_0 + b_0\theta + \sum_{n=1}^2(a_n \cos w\theta + b_n \sin w\theta))L, \quad (9)$$

where the coefficients  $a_n$ ,  $b_n$  and  $w$  can be defined by the calibration data as well. Therefore, the  $M_r(\theta, P_c)$  can be obtained by Eq. (10).

$$M_r(\theta, P_c) = M_r(\theta) + M_r(P_c). \quad (10)$$

By combining Eqs. (8), (9) and (10), it is then possible to determine the stiffness  $K(\theta)$ . All the parameters in both kinematic and stiffness models can be determined by the calibration process. The result of the calibration is shown in Table 1.

### 3.4. Calibration of model coefficients

For calibrating the coefficients of the kinematics model, three groups of calibration data are used to fit the model with a Matlab script. These three groups are based on the experimental data when the bending angles are 15 degrees,

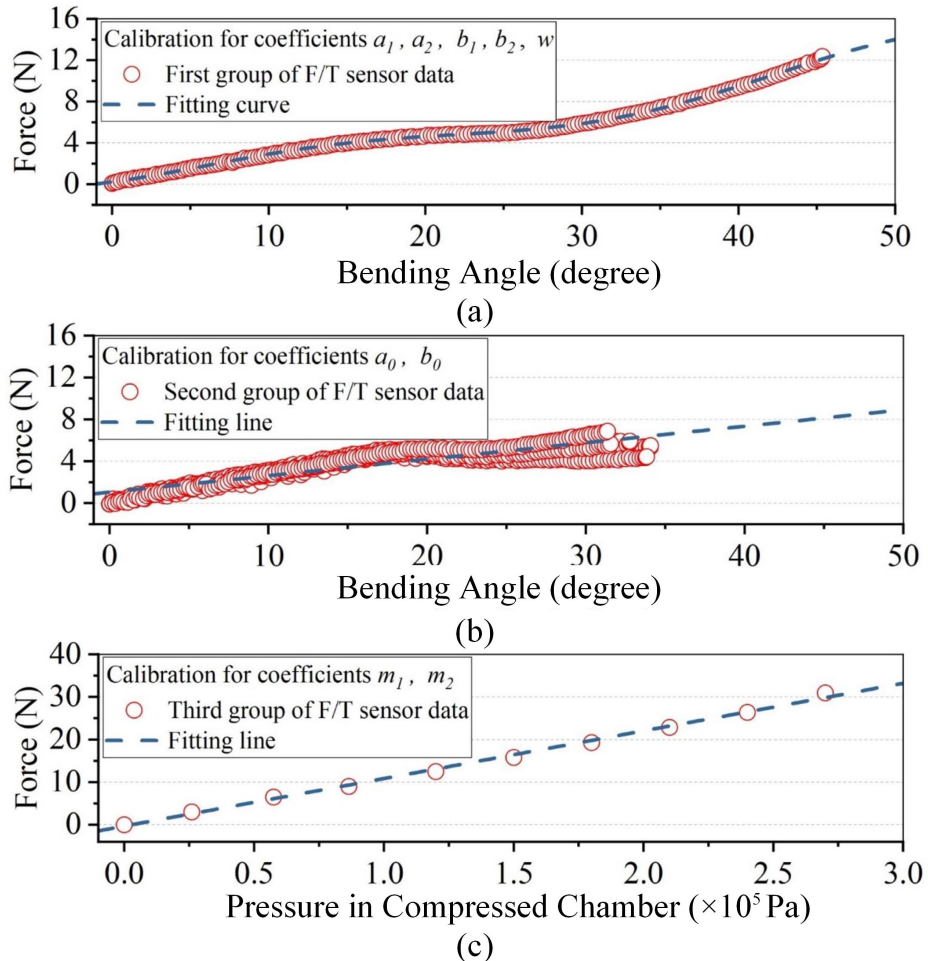


Figure 6. (a) Calibration for the coefficients  $a_1$ ,  $a_2$ ,  $b_1$ ,  $b_2$ , and  $\omega$  by fitting the F/T sensor data when the chamber is at 0 Pa pressure. (b) Calibration for the coefficients  $a_0$  and  $b_0$  by fitting the second group of F/T sensor data. (c) Calibration for the coefficients  $m_1$  and  $m_2$  by fitting the third group of F/T sensor data.

30 degrees, and 45 degrees, respectively. For the calibration of the coefficients in the stiffness model, a single chamber with the hinge and linear rail is used with the F/T (Force/Torque) sensor to measure the resistance force data of the compressed chamber. When the chamber's pressure is 0 Pa, the F/T sensor can record the first group of output torque as the bending angle changes from 0 to 48 degrees. Coefficients  $a_1$ ,  $a_2$ ,  $b_1$ ,  $b_2$ , and  $\omega$  in the Fourier expansion can be calibrated by the first group of torque data from the F/T sensor as shown in Fig. 6 (a). Next, the chamber is inflated by  $0.5 \times 10^5$  Pa to  $1.5 \times 10^5$  Pa in  $0.5 \times 10^5$  Pa steps to determine the output force data using the F/T sensor. Data at every pressure, minus the data at 0 Pa, is adjusted to start at the original point so coefficients  $a_0$  and  $b_0$  can be calibrated using this second group of data, as shown in Fig. 6 (b). The starting point of the data at each pressure is then extracted as the third group of data to calibrate the coefficients  $m_1$  and  $m_2$ , as shown in Fig. 6 (c). The setup for the calibration process is shown in Fig. 7 (a) and the calibration results are shown in Fig. 7 (b).

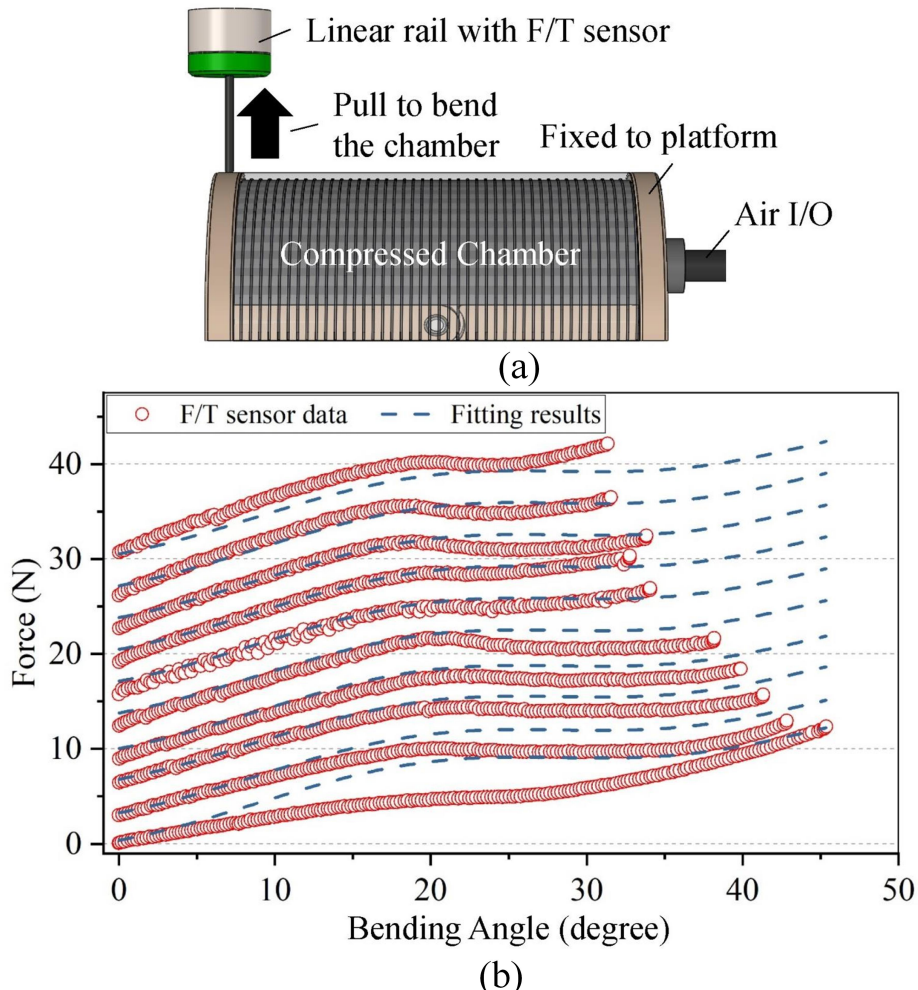


Figure 7. (a) Setup for obtaining the calibration data. (b) Calibration results.

#### 4. Experimental protocol, setup and results

##### 4.1. Experimental protocol and setup

###### 4.1.1. Experiment 1 - Bending angle evaluation and kinematic model verification

An electro-magnetic tracking system is used to monitor the bending angle under the different combinations of pressure in the two chambers. Due to the symmetry of the joints, only one bending direction needs to be evaluated,

Table 1. Nonlinear model results.

Parameter	Value	Unit	Parameter	Value	Unit
$n_0$	4.601e-10	—	$a_0$	7.542	—
$A_{P_0}$	2.395e-4	$m^2$	$a_1$	-2.183	—
$A_i$	1.793e-4	$m^2$	$a_2$	-1.304	—
$a$	0.018	$m$	$b_0$	0.054	—
$\bar{u}$	0.207	MPa	$b_1$	-4.935	—
$n_1$	100.844	—	$b_2$	0.427	—
$n_2$	1.4	—	$m_1$	1.159e-4	—
$L_m$	0.009	$m$	$m_2$	-0.129	—
$L$	0.049	$m$	$w$	0.067	—

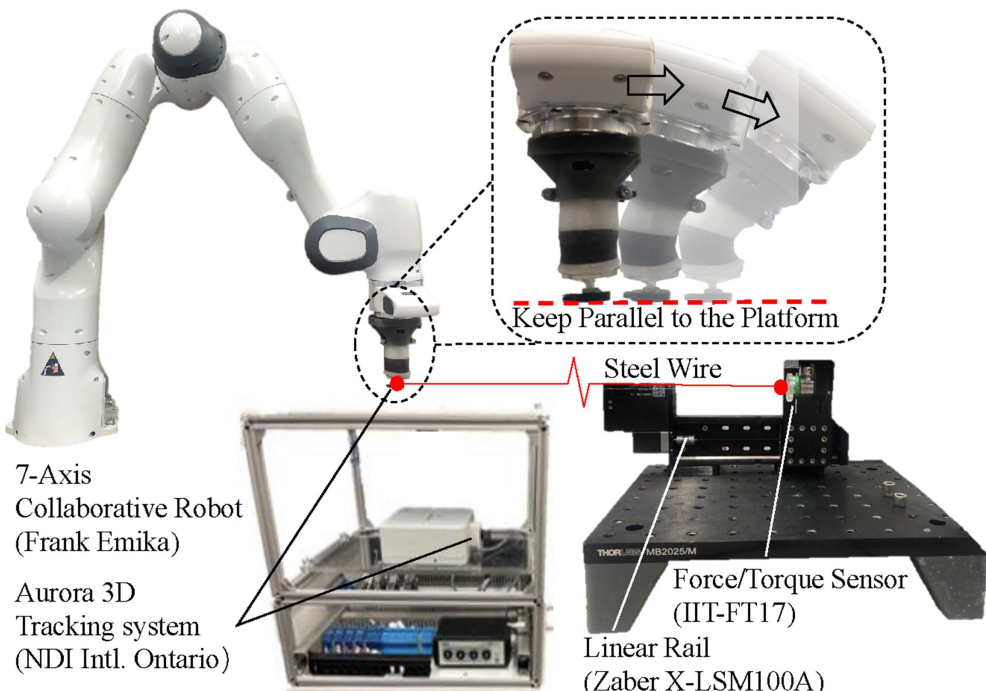


Figure 8. Setup for Experiment 2 - Stiffness evaluation: The joint prototype was fixed at the end of the 7-axis collaborative robot (Franka Emika) to ensure the top of the joint remained parallel to the platform during the experiment. The linear rail (Zaber X-LSM100A), equipped with a 6-axis F/T sensor (IIT-FT17), is used to generate the displacement on demand and record the force during the displacement. An inextensible steel wire with a 0.2 mm diameter and 1200 mm length is used to connect the F/T sensor and the top of the joint. The Aurora 3D Tracking system (NDI Intl. Ontario, Canada) measures the bending angle change generated by the displacement from the linear rail.

which means the pressure in one chamber was always higher than in the other. Therefore, the command pressure value in the two chambers were combinations of 0 and  $1.5 \times 10^5$  Pa in  $0.5 \times 10^5$  Pa steps ( $P_1 \geq P_2$ ). To verify the kinematic model, the same values of  $P_1$  and  $P_2$  are applied to (5) to calculate the bending angle numerically using Matlab. The parameters during the calculation are shown in Table 1.

The setup includes the Aurora 3D Tracking system (NDI Intl. Ontario, Canada) measuring the bending angle. This allows the motion of the tip sensor in the magnetic field to be recorded in quaternions. A Matlab script then converts the quaternions to a bending angle. The position and orientation tracking errors of the Aurora system (using a 6 DoF sensors and a cubic volume) are less than 0.48 mm and 0.30°, respectively.

#### 4.1.2. Experiment 2 - Stiffness evaluation and stiffness model verification

The joint is fixed at the end of a multi-axis robot to ensure the top of the joint remained parallel to the platform at any bending angle. A linear rail with a force sensor applied a displacement on the top of the joint using an inextensible steel wire. The resolution of the force sensor is 10 mN for each axis. The electromagnetic tracking sensor at the top of the joint recorded the change of the bending angle caused by the displacement of the linear rail, and the force sensor recorded the applying force. Finally, the force was transferred into the torque by the geometrical relationship. The torque and the changing angle indicate the stiffness of the joint at different bending angles. As in the bending angle evaluation, the command pressure value in the two chambers were combinations between 0 and  $1.5 \times 10^5$  Pa in  $0.5 \times 10^5$  Pa steps ( $P_1 \geq P_2$ ). To verify the stiffness model, the value of  $P_1$  is set as  $P_c$  in (10), and  $\theta$  and  $\Delta\theta$  are determined by the data from the electromagnetic tracking sensor. Matlab is used to calculate the stiffness, and the parameters during the calculation are shown in Table 1.

The setup shown in Fig. 8 evaluates the stiffness of the joint prototype. The prototype is fixed at the end of a Franka Emika cobot (Germany) to ensure that the top of the joint will remain parallel to the platform at each bending angle. An Aurora 3D Tracking system is used to check the prototype's initial position after each adjustment of the collaborative robot and to measure the change of bending angle generated by the displacement from the linear rail. The linear rail (Zaber X-LSM100A) is equipped with a 6-axis F/T sensor (Istituto Italiano di Tecnologia, Via Morego, Italy), and it is used to generate the displacement on demand and record the force during the displacement. An inextensible steel wire with a 0.2 mm diameter and 1200 mm length is used to connect the F/T sensor and the top of the joint. The wire is relatively light so the mass itself will not significantly influence the force.

#### 4.1.3. Experiment 3 - Output force evaluation

For evaluating the output force of the proposed joint prototype, the tip of the joint is placed on the surface of a Force/Torque (F/T) sensor (IIT, Genova, Italy). One of the chambers will be inflated by the pressure from 0 Pa to  $1.5 \times 10^5$  Pa. Thus, the force generated by the joint will be recorded by the F/T sensor.

The setup in Fig. 12 can record the force generated by the joint prototype. The prototype is fixed on a rigid platform and the tip of the joint is located on the surface of an F/T sensor (IIT-FT17) mounted on the linear rail. This linear rail can adjust the initial gap between the tip and the force sensor.

#### 4.1.4. Experiment 4 (Application) - Output force control

In an application scenario, we demonstrate the advantages of our proposed stiffness-controllable joint in terms of dynamical constant force output. The joint is actuated to exert a constant force on a rotating target plate. The F/T sensor will record the contact force (i.e. output force of the joint) in real-time.

As shown in Fig. 9 (a), the proposed joint is connected to a rigid link resulting in a joint-link motion unit. An F/T sensor is mounted on the top of the unit to record the output force. The target plate is connected to a Dynamixel motor so that the rotational trajectory is the same as the one of the motion unit tip. As shown in Fig. 9 (b), the Dynamixel motor is controlled to achieve a rotational velocity of 1°/s for up to 30 seconds. In this experiment, an actuation velocity of 1°/s was chosen to eliminate the dynamic response of the joint actuation, which is significantly influenced by the performance characteristics of the pressure regulator and the hysteresis properties of the silicone material. This decision was made based on the understanding that a controlled lower actuation speed (i.e. 1°/s for instance) facilitates the achievement of a stable and uniform force output. By adopting a reduced velocity, we aim to showcase the capability of our joint prototype to produce a precise and consistent force output. In the meantime, the proposed joint is actuated to generate the output force applied on the target plate. The offset pressure will determine

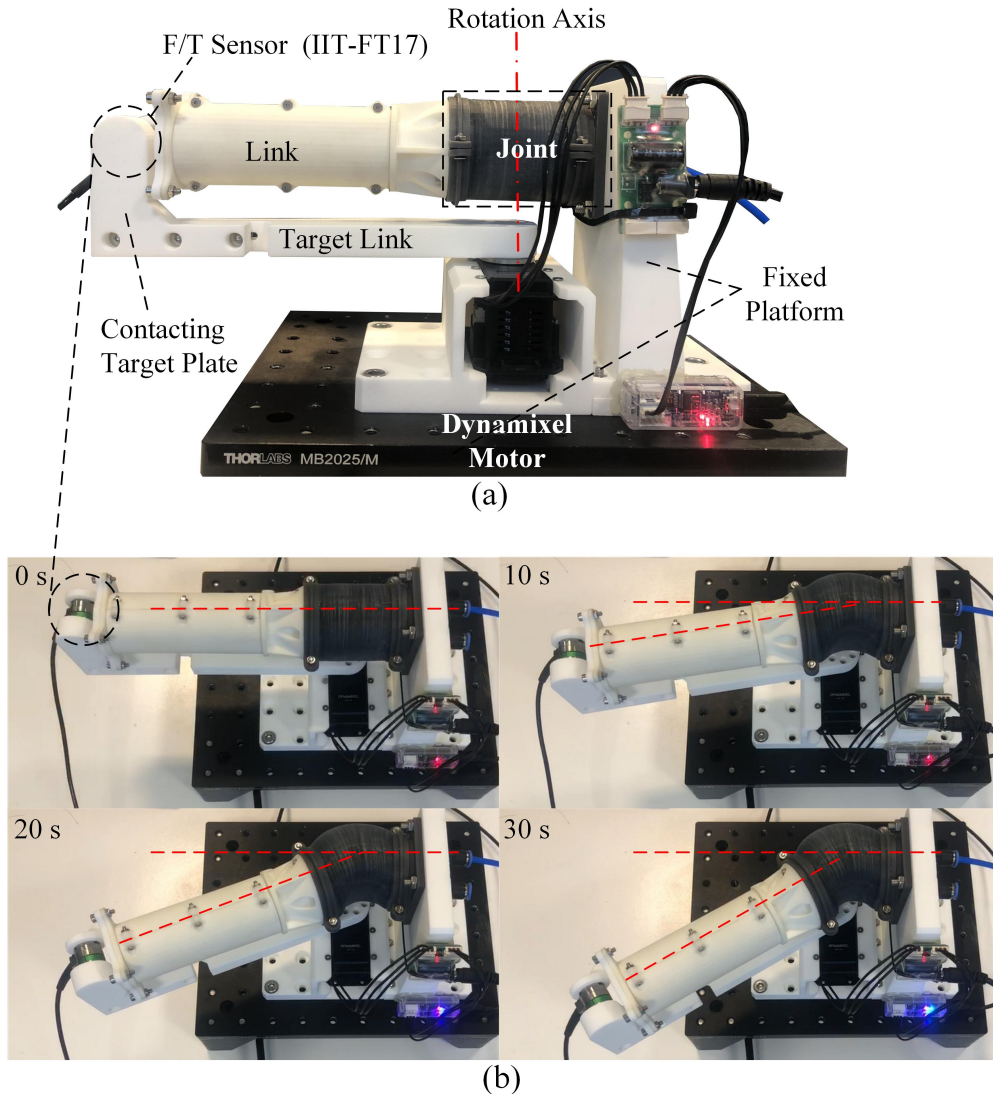


Figure 9. (a) Setup of the experiment 4. The proposed joint is connected by a rigid link with an F/T sensor on the tip. The sensor will contact the target plate when the joint is actuated, while the target plate is rotating by the control of the Dynamixel motor with a speed of  $1^\circ/\text{s}$ . Thus, the F/T sensor can record the contacting force during the rotating motion, which represents the output force of the joint. In this scenario, it can show how easily the proposed joint can achieve a constant force output to the target and change the interaction force as demanded. (b) The process of the application. The target plate is rotating at a speed of  $1^\circ/\text{s}$ , while the proposed joint is actuating the sensor on the tip to output a constant force on the target plate.

the value of the output force, while the ramp is the required pressure for the joint to achieve the bending angle itself (it can be calculated by the kinematic model proposed in Section 3.2).

#### 4.2. Experimental results

##### 4.2.1. Experiment 1 results

In Fig. 10 (a), the solid lines represent the experimental result of the bending angle response. For example, the solid red line represents the pressure in chamber 2 remaining 0 Pa; as the pressure in chamber 1 increases from 0 Pa to  $1.5 \times 10^5$  Pa in the  $0.5 \times 10^5$  Pa increments, the bending angle increases from 0 degrees to 48.795 degrees, which means the joint can reach a bending angle of approximately 100 degrees in total using the symmetrical principle.

Compared to the maximum bending angle (i.e. 90 degrees) achieved by a similar size joint proposed in [25], the bending angle range of our joint is around 10 degrees wider. The other solid lines in different colors represent the bending angle response to different pressure. The results indicate that the increase in the bending angle is not a strictly linear process. The error bar shows the measurement error of the bending angle. The light dots represent the result of the kinematic model under the same pressure as the experiments, which illustrates the model results are more linear than the experimental results.

Fig. 10 (b) shows the deviation between the kinematic model and the experiment result. According to the calculation, the average deviation is 0.927 degrees and the average deviation rate is 1.93%, having a smaller error compared with a bending actuator with the same actuation principle (i.e. 3.7%) proposed in Polygerinos' paper [23]. Hence, the kinematic model proposed in this paper can be considered a reasonable model to predict bending behavior. Besides, the result of the bending angle is presented in Fig. 11 (a) as a contour map as well. The horizontal and vertical axes represent the pressure in two chambers, respectively, while the contour line represents the bending angle value. Since only half of the experiments (i.e.  $P_1 \geq P_2$ ) were carried out, the other half of the results are depicted using the symmetrical principle.

#### 4.2.2. Experiment 2 results

Fig. 10 (d), the experimental result of the stiffness evaluation is presented by the set of the rigid curves; for instance, the red line shows the change of prototype stiffness when the pressure in chamber 2 remains 0 Pa and the pressure in chamber 1 increase from 0 Pa to  $1.5 \times 10^5$  Pa. The error bar represents the measurement error of the stiffness. Fig. 10 (c) shows the deviation of the stiffness model. The unmatched deviation mainly occurs when  $P_2 = 0 \times 10^5$  Pa. The stiffness model has a maximum deviation when  $P_1 = 3 \times 10^5$  Pa and  $P_2 = 0 \times 10^5$  Pa, which is 9.219 N.mm/degree. While the average deviation is 5.394 N.mm/degree and the deviation rate is 5.25%, Compared to the force model error (i.e. 10.3%) in Polygerinos' paper [23] again, it can be considered a better stiffness model.

Fig. 11 (b) depicts the stiffness range that the prototype can achieve. The map shows that the minimum stiffness is 26.56 N.mm/degree when  $P_1 = 0 \times 10^5$  Pa,  $P_2 = 15 \times 10^5$  Pa or  $P_2 = 0 \times 10^5$  Pa,  $P_1 = 15 \times 10^5$  Pa, and the maximum stiffness is 102.59 N.mm/degree when  $P_1 = P_2 = 3 \times 10^5$  Pa. Besides, it is observed that the antagonistic actuation principle leads to a maximum variable range of stiffness from 35.42 N.mm/degree to 102.59 N.mm/degree when the bending angle remains 0 degree. Besides, when the prototype keep the stiffness of 102.59 N.mm/degree, the maximum output torque would be 4890 N.mm. In comparison, the novel soft joint discussed in this research can achieve much higher torque values (4890 N.mm compared to 400 N.mm reported in [25]) due to the antagonistic actuation principle and reinforced structure.

#### 4.2.3. Experiment 3 results

Fig. 12 shows the result for the output force evaluation. The red curve represents the force generated by the joint when it is inflated, and the blue curve represents deflation. The shadow of the curves is the measurement error. The results show that the output force can reach around 20 N when the actuation pressure is  $1.5 \times 10^5$  Pa. During inflation and deflation, the force curve keeps approximate linearity well. There is a minor hysteresis at the beginning but disappears when pressure is higher than  $0.5 \times 10^5$  Pa.

#### 4.2.4. Experiment 4 results

With the offset pressure  $0.5 \times 10^5$  Pa,  $11.5 \times 10^5$  Pa, and  $15.5 \times 10^5$  Pa, the proposed joint achieves three different constant force outputs (see the solid curves in Fig. 13), which are around 2.1 N, 4 N, and 6.4 N during a 30 seconds rotation. The fluctuations are 0.227 N, 0.356 N, and 0.321 N. The fluctuating rate is reasonably low considering that only the kinematic model is used here to achieve a dynamical output force control for the joint. The results prove that the proposed joint can realise a constant force output (i.e., setting the actuation pressure by kinematic model) and change an on-demand interaction force (i.e. changing the offset pressure).

### 4.3. Discussion

In Experiment 1 and 2, it is observed the non-linearity of the bending and stiffness behaviour is significant, which can be explained by the buckling of the chamber. During the bending motion, one of the chambers will be compressed by the torque generated from the other extended chamber. Like the buckling of columns under the compression,

the semi-cylindrical chamber under the compression will have elastic bending at the beginning, then when the angle reaches a critical level (around 20 degrees for the proposed prototype), the wall of the chamber suddenly folds into the interior, leading to the sharp decrease of the torque applied on the hinge. It is observed in Fig. 10 (a) that the bending angle curve has a steeper slope of around 20 degrees, as well as a significant drop in the stiffness curve around the third point shown in Fig. 10 (d) due to the same reason. Since the kinematic model is built by a linear equation, the deviation between the experiment and the model could be explained by the buckling as well.

We compared our stiffness-controllable joint with a commercially available, electromagnetic actuator (i.e. Motor Dynamixel 430 [42] and joint mechanisms from the literature [23, 25, 29], considering various parameters such as maximum bending angle, force output capabilities, variable stiffness functionality, methods for stiffness adjustment, physical dimensions, and bending modality. The comparative results, detailed in Table 2, show that our joint design offers a moderate maximum bending angle and physical dimensions while achieving a competitive force output. It is

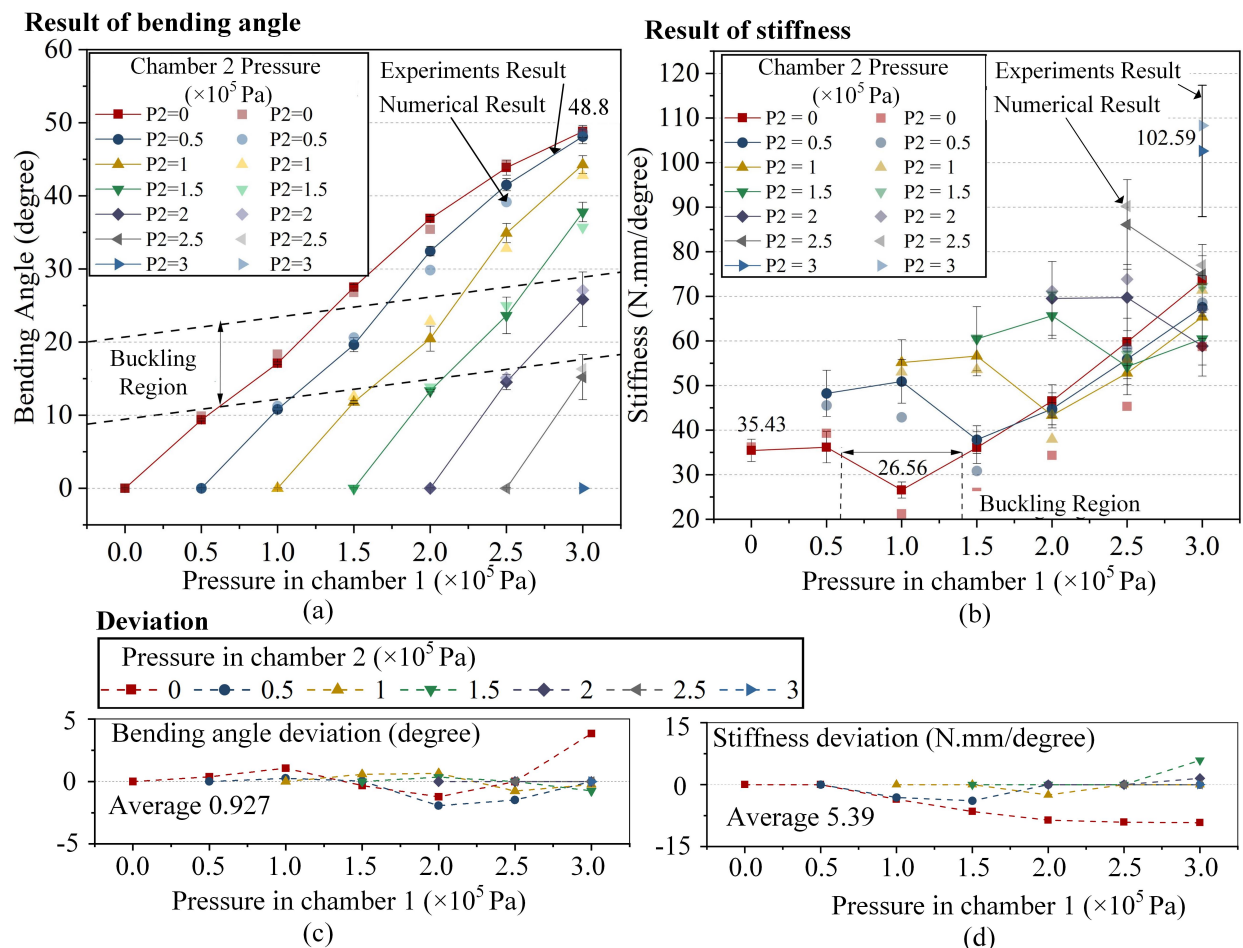


Figure 10. (a) Results of Experiment 1 - The solid line represents the experimental result of the bending angle response when pressurised between 0 and  $3 \times 10^5$  Pa in  $0.5 \times 10^5$  Pa ( $P_1 \geq P_2$ ). The maximum bending angle is 48.8 degrees when actuated with  $3 \times 10^5$  Pa air pressure. The error bar shows the deviation of the measurement. The light dots represent the result calculated by the numerical bending model under the same pressure as the experiments. (b) The curve shows the deviation between the model and experimental result of bending angle. (c) The curve shows the deviation between model and experimental results of stiffness. (d) Result of Experiment 2 - The curves represent the stiffness response when pressurized between 0 and  $3 \times 10^5$  Pa in  $0.5 \times 10^5$  Pa increments ( $P_1 \geq P_2$ ); the dots in each curve are at the same pressure value of  $P_2$ . The minimum stiffness is 26.56 N.mm/degree when  $P_2 = 0$  Pa,  $P_1 = 1 \times 10^5$  Pa, and the maximum stiffness is 102.59 N.mm/degree when  $P_1 = P_2 = 3 \times 10^5$  Pa. The error bar shows the deviation of the measurement. The light dots represent the result calculated by the stiffness model under the same pressure as the experiments.

observed that only actuators employing alternative methods surpass the new joint in terms of force output (it is worth mentioning that the actuator has a larger dimension, notably with actuator lengths exceeding 150 mm). Furthermore, these actuators are generally limited to unidirectional bending, in contrast to the capability of our joint for more versatile bidirectional bending. Regarding variable stiffness, the performance of our joint is comparable to actuators utilising similar antagonistic actuation principles, albeit it is surpassed in stiffness capabilities by those employing stiffness-controllable material such as jamming methods.

Elevating the actuation pressure leads to a proportional increase in the output force. This increase in force would require the integration of a reinforced layer, capable of withstanding a greater extension force. Also, the central rigid hinge is subjected to increased forces along its axis, setting a practical limit to the extent to which actuation pressure can be increased without risking structural failure in both the reinforced layer and the rigid hinge. Nonetheless, according to numerical modelling, there is potential to further enhance the maximum force output. Eq. 7 shows that the output force,  $F_o$ , can be described by Eq. 11.

$$F_o = F_{p1} - F_i(\theta) - \frac{M_r(\theta)}{L_m} \quad (11)$$

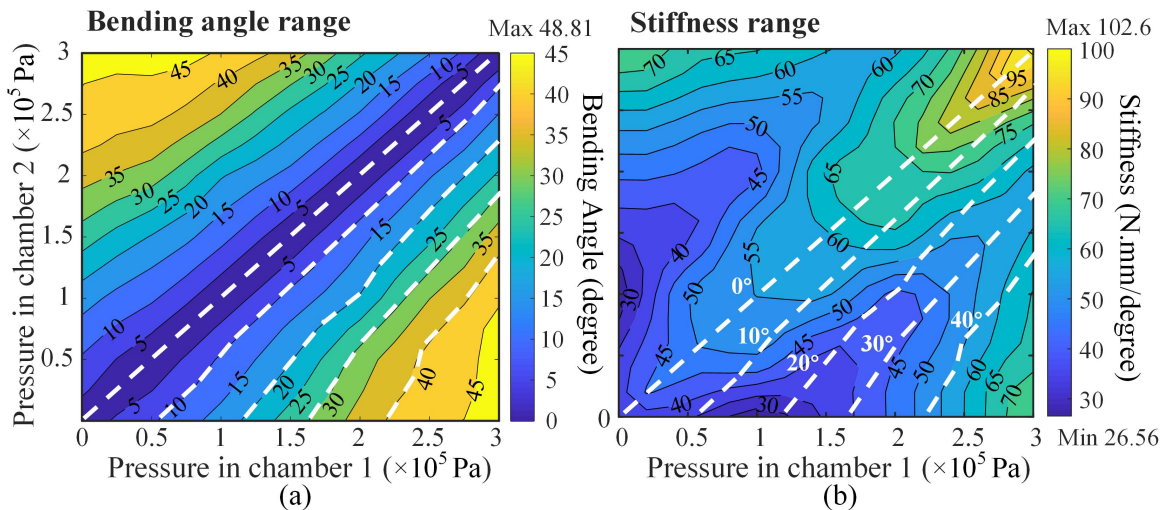


Figure 11. Results of Experiments 1 and 2: Contour map (a) shows the range of the bending angle, and contour map (b) shows the stiffness the prototype can achieve when pressurized between 0 and  $1.5 \times 10^5$  Pa in chambers 1 and 2. The white dotted lines in map (b) are the same contour lines of the bending angle.

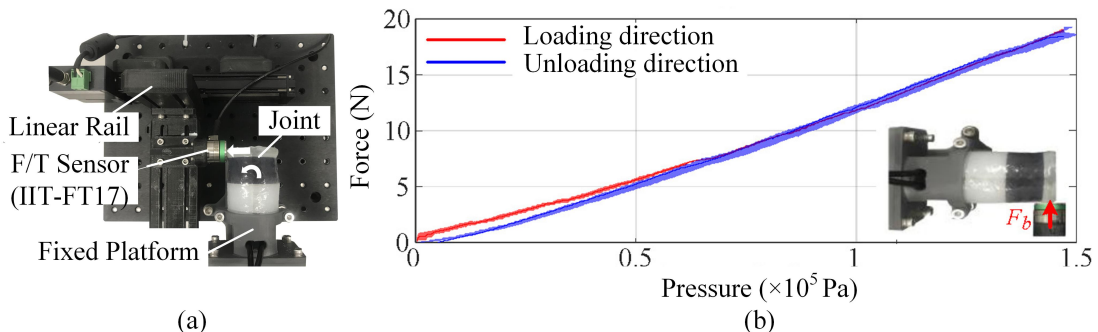


Figure 12. The result for the output force evaluation. The red curve represents the force generated by the joint when it is inflated, and the blue curve represents deflation. The shadow of the curves is the measurement error. The results show that the output force can reach around 20 N when the actuation pressure is  $1.5 \times 10^5$  Pa.

where the  $F_{p_1}$  is determined by the joint dimensions  $a, b, t$  and  $F_i$  is determined by the initial shear modulus  $\bar{\mu}$ . The parameters  $a, b$ , and  $t$  mainly affect the cross-section area of the chambers, thus when the cross-section area increases, the output force will increase accordingly. Besides, the decrease of the shear modulus  $\bar{\mu}$  will reduce the resistant force of the chamber extension. This implies that using a softer material to construct the chamber will also increase the output force. However, it is important to note that a softer material may pose a potential problem – in particular, the side walls of the chambers may extend between two reinforced threads, forming noticeable bubbles and causing chamber failure. Therefore, a relatively high shear modulus of material is essential for constructing the chambers. Furthermore, beyond increasing the maximum output force, there exists an opportunity to improve the variation in stiffness. This stiffness variation is dependent on the force produced by both chambers, in adherence to the antagonistic principle. Thus, the strategies employed to enhance the output force are equally applicable for amplifying stiffness variation. It is critical to acknowledge, however, that increasing the antagonistic force results in a greater axial force being exerted on the rigid central hinge than that observed during efforts to boost output force alone. As a consequence, adjusting stiffness variation must be accompanied by considerations for reinforcing the structural integrity of the rigid central hinge to accommodate these increased forces.

Looking into the result of the application scenario, our joint has a significant advantage in terms of constant output force control. A constant force output can be achieved (i.e., setting the actuation pressure by the kinematic model)

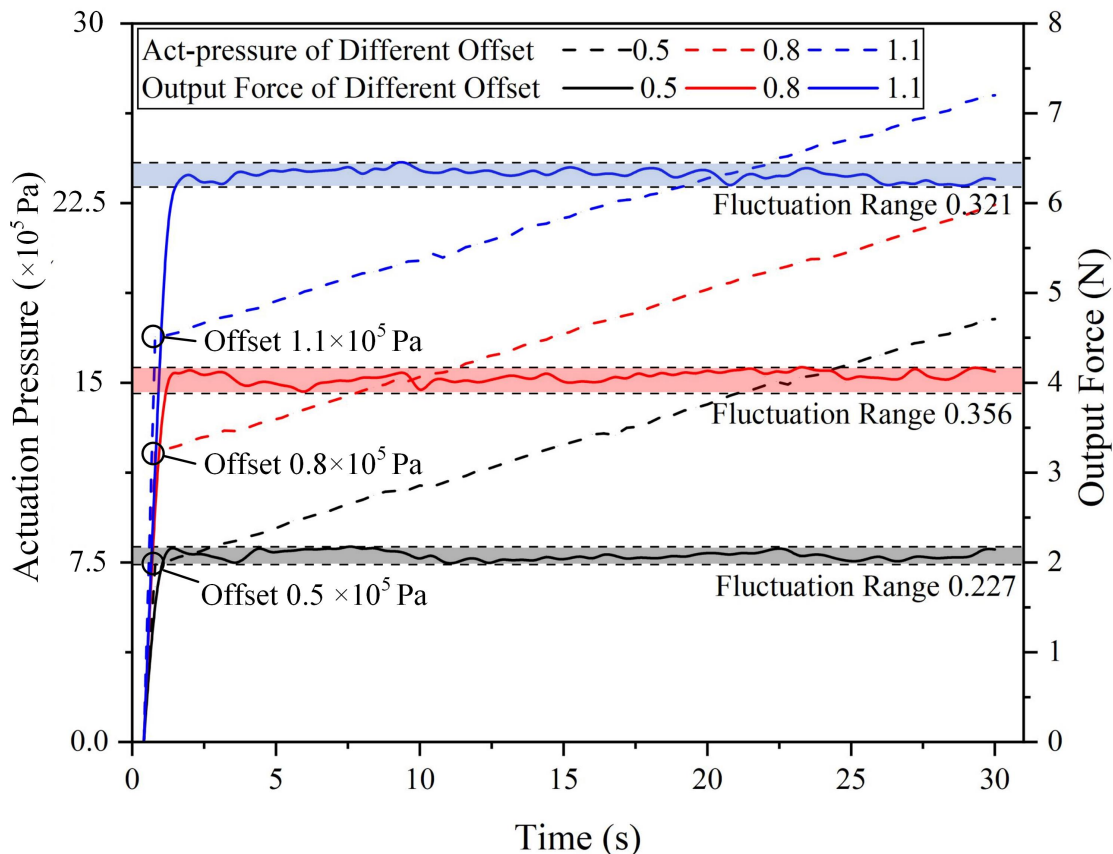


Figure 13. The output recording of the experiment 4. The dotted curves show the actuation pressure of the proposed joint. The offset pressure determines the amount of the output force, while the ramp is the needed pressure for the joint to achieve the bending angle itself (it can be calculated by the kinematic model proposed in the Modelling section). The solid curves in Fig. 13 show the output force results. With the offset pressure  $0.5 \times 10^5$  Pa

,  $11.5 \times 10^5$  Pa, and  $15.5 \times 10^5$  Pa, the proposed joint achieve three different constant force output, which is around 2.1 N, 4 N, and 6.4 N during the whole 30 seconds rotation. The fluctuations are 0.227 N, 0.356 N, and 0.321 N.

and change an on-demand interaction force (i.e., changing the offset pressure), which is usually implemented through impedance control [43] when the joint is an electrical motor. This advantage will be helpful for a collaborative robot equipped with the proposed joint to achieve output force control easier than any electrical motor. In addition, the observed fluctuations in constant force values will need to be considered (in particular, 0.321 N, 0.356 N, and 0.227 N). The first potential factor contributing to these fluctuations could be the measurement resolution, as the F/T sensor has an error of 10 mN. However, given that the fluctuation range is 0.3 N, the impact of this factor might be relatively low. Secondly, fluctuations in actuation pressure from the regulator should be taken into account. It is evident that the dotted lines (showing the actual actuation pressure based on regulator feedback) display several oscillations along the slope, resulting in a significant fluctuation in force output. Thirdly, despite choosing a slow speed of motor rotational velocity at 1°/s, the hysteresis of the silicone material and the stability of motor rotation can still influence the fluctuation in output force. In summary, to enhance the stability of the output force, improvements can be made to the regulator's performance, and efforts can be directed towards adding compensation to the output force model and control to mitigate the effects of silicone material hysteresis.

## 5. Cobot with variable stiffness joints: a case study

To showcase the variable stiffness capabilities of the proposed joint, a serial robot was created using two different-sized joints, a base rotation joint, and two links, as shown in Fig. 14 (a). The first joint has a diameter of 50 mm, while the second joint has a diameter of 40 mm. The lengths of each component are also indicated in Fig. 14 (a). By leveraging the numerical kinematic and stiffness model presented in Section 3.3, the end effector of the serial robot is programmed to reach the same target position with varying levels of stiffness. In this case study, the two joints were actuated to achieve bending angles  $\theta_1$  and  $\theta_2$ , but with different joint stiffness values, namely  $K'_1$ ,  $K'_2$ ,  $K''_1$ , and  $K''_2$ , where  $K''_1 > K'_1$  and  $K''_2 > K'_2$ . In another set of experiments, a 200-gram weight was applied to the robot's end effector each time. Consequently, it was observed that the deflection of the robot's end effector was smaller when employing higher joint stiffness, as compared to the case with lower stiffness values (i.e.,  $D_2 > D_1$ ). This observation highlights the significant advantage of the proposed joints in enhancing the robot's loading capacity through the antagonistic actuation principle, in particular, when compared to systems utilizing purely soft joints or joints lacking variable stiffness.

A further experiment was conducted to demonstrate the compliance, flexibility, and safety of the robot equipped with the proposed joints. The robot was activated to reach a target position, with the joint angles set as  $\theta_{d1}$  and  $\theta_{d2}$ , and corresponding stiffness values of  $K_1$  and  $K_2$  in the two joints. However, a human hand was deliberately placed intersecting the robot's path. During the interaction with the obstacle, it was observed that the joints were able to adjust their bending angles based on the stiffness settings. As a result, the actual angles reached due to the obstacle's presence were denoted as  $\theta_{r1}$  and  $\theta_{r2}$ . The force exerted on the obstacle during this interaction can be calculated using Eq. (12).

$$F_c = L_2 K_2 (\theta_{d2} - \theta_{r2}). \quad (12)$$

From Eq. (12), it can be concluded that the contacting force is significantly reduced when the joint stiffness is set to a lower value. By appropriately setting the working stiffness of the robot equipped with our joints, the robot can

Table 2. Comparison between a commercially available actuator, joints found in the literature and our proposed stiffness-controllable joint.

Source	MA (°)	MF (N)	SV (times)	SVM	Dimensions (mm)	Bending Type
Motor Dynamixel 430 [42]	360	14.28	—	—	28.5 × 46.5 × 34	Bidirectional
L. Paterno et al. [23]	170	1.4	3	Antagonistic Actuation	10 × 15 (C)	Bidirectional
J. Fras et al. [25]	85.9	10	—	—	36 × 36 (C)	Unidirectional
X. Zeng et al. [29]	340	35	75	Jamming	150 × 30 × 20	Unidirectional
Proposed Joint	100	20	3	Antagonistic Actuation	49 × 35 (C)	Bidirectional

MA: Maximum Angle; MF: Maximum Force; SV: Stiffness Variation; SVM: Stiffness Variation Method; (C): Cylinder

successfully achieve task requirements while maintaining a low contact force during interactions. This characteristic allows the robot to achieve both force and position control simultaneously, eliminating the need for sensors and complex compliance control methods.

## 6. Conclusion

This paper proposes a novel soft joint with a compact structure (i.e. 49 mm height and 38 mm diameter) based on a rigid central hinge and silicone chambers reinforced by a fibre layer. It is made with a high percentage (i.e. over 80% in volume) of soft materials that provide inherent safety. The kinematic model and stiffness model for

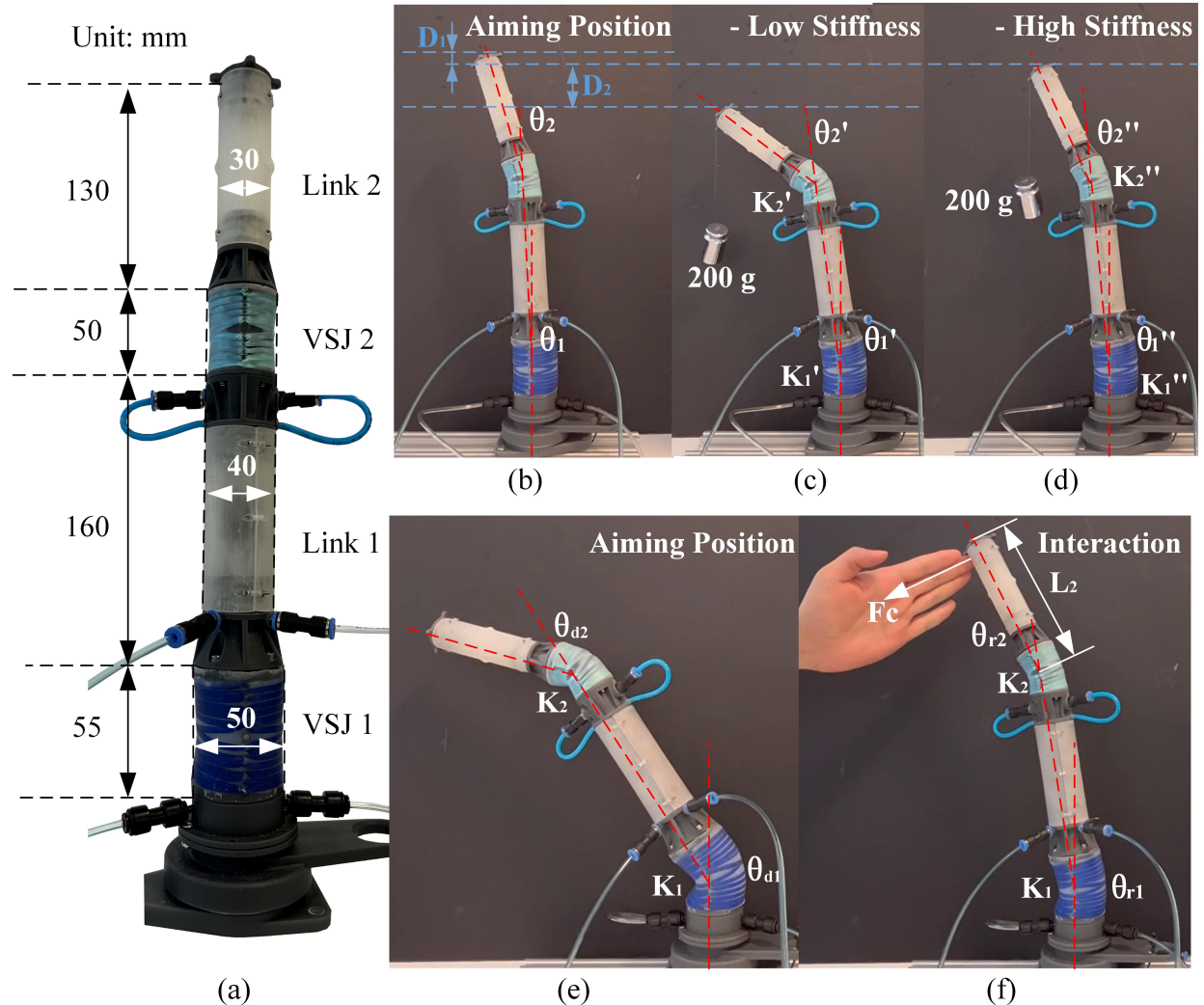


Figure 14. (a) Dimension of serial robot equipped with two variable stiffness joints. (b) The robot aims at a target position without any external load. The bending angles are denoted as  $\theta_1$  and  $\theta_2$ . (c) The robot is loaded with a 200-gram weight with low joint stiffness. The true bending angles are observed as  $\theta'_1$  and  $\theta'_2$ . Notably, significant deflection is observed at the end effector. (d) The robot carries a 200-gram weight, but the two variable stiffness joints (VSJs) possess high stiffness. The true bending angles are represented as  $\theta''_1$  and  $\theta''_2$ , resulting in minor deflection at the end effector. (e) The robot is shown in its actuated state, moving towards the target position. The bending angles are set as  $\theta_{d1}$  and  $\theta_{d2}$ , with corresponding stiffness values of  $K_1$  and  $K_2$ . (f) Interaction between the robot's tip and a human hand when reaching the target position. Notably, the robot adapts to the obstacle's presence without exerting a significant force. The contacting bending angles are represented as  $\theta_{r1}$  and  $\theta_{r2}$ , while the contact force with the obstacle is denoted as  $F_c$ .

this joint are proposed and verified through testing. These experiments demonstrate that the soft joint can achieve a bending angle of 48.8 degrees in one direction and a bending angle of approximately 100 degrees in total with a fixed center like a traditional joint. In particular, this novel joint is able to benefit from the antagonistic activation principle and significantly change its stiffness (i.e. maximum variable stiffness range is from 35.42 N.mm/degree to 102.59 N.mm/degree). In addition, the average deviation between the proposed model and experimental data is 1.93% regarding the kinematic model and 4.49% regarding the stiffness model. Our joint can achieve 20 N output force at  $1.5 \times 10^5$  Pa pressure. The constant force output experiments proves the advantage of our joint achieving a constant force output in an effective way. Our case study includes a serial cobot equipped with the proposed joints. Here, we highlight the significant advantages of this type of robot in terms of enhanced loading capacity through the antagonistic actuation principle as well as safe human-robot interaction facilitated by their compliance and flexibility.

In future work, the proposed joint will be further developed into different types, enabling not only bending but also rotation. These joints will then be integrated with variable stiffness links to create a multi-degree-of-freedom stiffness-controllable collaborative robot. This advancement aims to enable even safer human-robot interactions while achieving performance levels comparable to conventional motor-based cobots.

## Acknowledgements

This work is supported by the Engineering and Physical Sciences Research Council (grant numbers: EP/R037795/1, EP/S014039/1 and EP/V01062X/1), the Royal Academy of Engineering (grant number: IAPP18-19\264), and UCL Mechanical Engineering.

## References

- [1] A. J. Baerveldt, A Safety System for Close Interaction between Man and Robot, *IFAC Proceedings Volumes* 25 (30) (1992) 25–29.
- [2] I. D. Walker, D. M. Dawson, T. Flash, F. W. Grasso, R. T. Hanlon, B. Hochner, W. M. Kier, C. C. Pagano, C. D. Rahn, Q. M. Zhang, Continuum robot arms inspired by cephalopods 5804 (2005) 303–314.
- [3] J. E. Michaelis, A. Siebert-Evenstone, D. W. Shaffer, B. Mutlu, Collaborative or Simply Uncaged? Understanding Human-Cobot Interactions in Automation, *Proceedings of the 2020 CHI Conference on Human Factors in Computing Systems* 1 (12) (2020) 1–12.
- [4] G. Nabissi, S. Longhi, A. Bonci, ROS-Based Condition Monitoring Architecture Enabling Automatic Faults Detection in Industrial Collaborative Robots, *Applied Sciences* 13 (1) (2023) 143.
- [5] C. Gaz, M. Cognetti, A. Oliva, P. R. Giordano, A. De Luca, Dynamic identification of the franka emika panda robot with retrieval of feasible parameters using penalty-based optimization, *IEEE Robotics and Automation Letters* 4 (4) (2019) 4147–4154.
- [6] T. Hull, M. A. Minarcin, Considerations in Collaborative Robot System Designs and Safeguarding, *SAE International Journal of Materials and Manufacturing* 9 (3) (2016) 545–551.
- [7] J. Guo, Conceptual mechanical design of antagonistic variable stiffness joint based on equivalent quadratic torsion spring, *Science Progress* 103 (3) (2020) 1–49.
- [8] L. Huang, Y. Wei, X. Zhang, A Humanoid Soft Robotic Joint with Variable Stiffness, *Proceedings of IEEE Workshop on Advanced Robotics and its Social Impacts* (2019) 256–260.
- [9] X. Liu, Y. Liu, L. Zhang, Q. Cheng, Research on Variable Stiffness Actuator of Compliance Robot Joint, *2nd International Conference on Modeling, Simulation and Optimization Technologies and Applications* (2018) 299–304.
- [10] L. Fang, Y. Wang, Study on the stiffness property of a variable stiffness joint using a leaf spring, *Proceedings of the Institution of Mechanical Engineers Part C-Journal of Mechanical Engineering Science* 233 (3) (2019) 1021–1031.
- [11] Y. Yu, S. Wei, Q. Ji, Z. Yang, Design, Dynamics Analysis, and Real-Time Stiffness Control of a Variable Stiffness Joint, *Electronics* 2020 9 (6) (2020) 973.
- [12] M. Fanghua, B. Shusheng, C. Linkun, G. Hanjun, A novel design of planar high-compliance joint in variable stiffness module with multiple uniform stress leaf branches on rigid-flexible integral linkage, *Mechanism and Machine Theory* 174 (2022) 104889.
- [13] M. Zhang, L. Fang, F. Sun, X. Sun, Y. Gao, K. Oka, Realization of Flexible Motion of Robot Joint with A Novel Permanent Magnetic Spring, *2018 International Conference on Intelligence and Safety for Robotics, ISR 2018* (2018) 331–336.
- [14] C. Chaoyu, Z. Xianmin, Z. Benliang, L. Hai, Z. Hongchuan, W. Rixin, L. Jianhao, F. Ke, A novel analysis method for magnetically actuated soft origami mechanisms, *Mechanism and Machine Theory* 186 (2023) 105353.
- [15] N. Arman, B. Colin, S. A. Azita, Design, dynamic modeling, control and implementation of hydraulic artificial muscles in an antagonistic pair configuration, *Mechanism and Machine Theory* 153 (2020) 104007.
- [16] K. Bhaben, D. S.K., Nonlinear dynamics of a parametrically excited pneumatic artificial muscle (pam) actuator with simultaneous resonance condition, *Mechanism and Machine Theory* 135 (2019) 281–297.
- [17] W. Daoming, W. Yakun, Z. Bin, C. Zixiang, D. Huafeng, Development of an active and passive finger rehabilitation robot using pneumatic muscle and magnetorheological damper, *Mechanism and Machine Theory* 147 (2020) 103762.
- [18] A. Stilli, H. Wurdemann, K. Althoefer, A Novel Concept for Safe, Stiffness-Controllable Robot Links, *Soft Robotics* 4 (1) (2017) 16–22.
- [19] A. Stilli, L. Grattarola, H. Feldmann, H. A. Wurdemann, K. Althoefer, Variable Stiffness Link (VSL): Toward inherently safe robotic manipulators, *IEEE International Conference on Robotics and Automation* (2017) 4971–4976.

- [20] H. A. Wurdemann, A. Stilli, K. Althoefer, An Antagonistic Actuation Technique for Simultaneous Stiffness and Position Control, Lecture Notes in Computer Science 9246 (2015) 164–174.
- [21] J. M. Gandarias, Y. Wang, A. Stilli, A. J. García-Cerezo, J. M. Gómez-de Gabriel, H. A. Wurdemann, Open-loop position control in collaborative, modular variable-stiffness-link (vsl) robots, IEEE Robotics and Automation Letters 5 (2) (2020) 1772–1779.
- [22] M. Olszewski, Modern industrial robotics, Pomiary Automatyka Robotyka 24 (1) (2020) 5–20.
- [23] L. Paternò, G. Tortora, A. Menciassi, Hybrid Soft–Rigid Actuators for Minimally Invasive Surgery, Soft Robotics 5 (6) (2018) 783–799.
- [24] G. Bao, S. Cai, Z. Wang, S. Xu, P. Huang, Q. Yang, F. Xu, L. Zhang, Flexible pneumatic robotic actuator FPA and its applications, 2013 IEEE International Conference on Robotics and Biomimetics, ROBIO 2013 (2013) 867–872.
- [25] J. Fras, Y. Noh, H. Wurdemann, K. Althoefer, Soft fluidic rotary actuator with improved actuation properties, IEEE International Conference on Intelligent Robots and Systems (2017) 5610–5615.
- [26] W. Gaozhang, J. Shi, Y. Li, A. Stilli, H. Wurdemann, Characterisation of antagonistically actuated, stiffness-controllable joint-link units for cobots, 2023 IEEE International Conference on Robotics and Automation (ICRA) (2023) 655–661.
- [27] M. Su, R. Xie, Y. Zhang, X. Kang, D. Huang, Y. Guan, H. Zhu, Pneumatic Soft Actuator with Anisotropic Soft and Rigid Restraints for Pure in-Plane Bending Motion., Applied Sciences 15 (9) (2019) 2999.
- [28] J. Shi, W. Gaozhang, H. A. Wurdemann, Design and characterisation of cross-sectional geometries for soft robotic manipulators with fibre-reinforced chambers, 2022 IEEE 5th International Conference on Soft Robotics (RoboSoft) (2022) 125–131.
- [29] X. Zeng, H. Su, A high performance pneumatically actuated soft gripper based on layer jamming, ASME. J. Mechanisms Robotics 15 (1) (2023) 014501.
- [30] X. Zeng, C. Hurd, H. Su, S. Song, J. Wang, A parallel-guided compliant mechanism with variable stiffness based on layer jamming, Mechanism and Machine Theory 148 (2020) 103791.
- [31] G. B. Crowley, X. Zeng, H. Su, A 3d printed soft robotic gripper with a variable stiffness enabled by a novel positive pressure layer jamming technology, IEEE Robotics and Automation Letters 7 (2) (2022) 5477–5482.
- [32] W. H. Choi, S. Kim, D. Lee, D. Shin, Soft, multi-dof, variable stiffness mechanism using layer jamming for wearable robots, IEEE Robotics and Automation Letters 4 (3) (2019) 2539–2546.
- [33] A. Jiang, A. Ataollahi, K. Althoefer, P. Dasgupta, T. Nanayakkara, A variable stiffness joint by granular jamming, 36th Mechanisms and Robotics Conference, Parts A and B 4 (2012) 267–275.
- [34] K. Althoefer, Antagonistic actuation and stiffness control in soft inflatable robots, Nature Reviews Materials 3 (2018) 76–77.
- [35] B.-S. Kang, C. S. Kothera, B. K. S. Woods, N. M. Wereley, Dynamic modeling of mckibben pneumatic artificial muscles for antagonistic actuation, 2009 IEEE International Conference on Robotics and Automation (2009) 182–187.
- [36] A. Shiva, A. Stilli, Y. Noh, A. Faragasso, I. D. Falco, G. Gerboni, M. Cianchetti, A. Menciassi, K. Althoefer, H. A. Wurdemann, Tendon-based stiffening for a pneumatically actuated soft manipulator, IEEE Robotics and Automation Letters 1 (2) (2016) 632–637.
- [37] A. Stilli, E. Kolokotronis, J. Fraš, A. Ataka, K. Althoefer, H. A. Wurdemann, Static kinematics for an antagonistically actuated robot based on a beam-mechanics-based model, IEEE/RSJ International Conference on Intelligent Robots and Systems (IROS) (2018) 6959–6964.
- [38] F. Maghooon, A. Stilli, Y. Noh, K. Althoefer, H. A. Wurdemann, Tendon and pressure actuation for a bio-inspired manipulator based on an antagonistic principle, IEEE International Conference on Robotics and Automation (ICRA) (2015) 2556–2561.
- [39] A. Stilli, H. A. Wurdemann, K. Althoefer, Shrinkable, stiffness-controllable soft manipulator based on a bio-inspired antagonistic actuation principle, IEEE/RSJ International Conference on Intelligent Robots and Systems (2014) 2476–2481.
- [40] X. Chen, J. Yi, J. Li, J. Zhou, Z. Wang, Soft-actuator-based robotic joint for safe and forceful interaction with controllable impact response, IEEE Robotics and Automation Letters 3 (4) (2018) 3505–3512.
- [41] L. Marechal, P. Balland, L. Lindenroth, F. Petrou, C. Kontovounios, F. Bello, Toward a Common Framework and Database of Materials for Soft Robotics, Soft Robotics 8 (3) (2021) 284–297.
- [42] J. M. Gómez-de Gabriel, H. A. Wurdemann, Adaptive underactuated finger with active rolling surface, IEEE Robotics and Automation Letters 6 (4) (2021) 8253–8260.
- [43] F. J. Abu-Dakka, M. Saveriano, Variable Impedance Control and Learning—A Review, Frontiers in Robotics and AI 7 (2020) 177–187.